Title	First Incoherent Scatter Measurements and Adaptive Suppression of Field-Aligned Irregularities by the PANSY Radar at Syowa Station, Antarctic
Authors	Taishi Hashimoto, Akinori Saito, Koji Nishimura, Masaki Tsutsumi, Kaoru Sato, Toru Sato
Citation	Journal of Atmospheric and Oceanic Technology, 36(9), 1881-1888, 2019
Issue Date	2019-7-3
Type	Journal Article
URL	https://doi.org/10.1175/JTECH-D-18-0175.1
Right	
Textversion	publisher

First Incoherent Scatter Measurements and Adaptive Suppression of Field-Aligned Irregularities by the PANSY Radar at Syowa Station, Antarctic

TAISHI HASHIMOTO

National Institute of Polar Research, Tachikawa, Japan

AKINORI SAITO

Division of Earth and Planetary Sciences, Kyoto University, Kyoto, Japan

KOJI NISHIMURA AND MASAKI TSUTSUMI

National Institute of Polar Research, Tachikawa, Japan

KAORU SATO

Department of Earth and Planetary Science, The University of Tokyo, Tokyo, Japan

TORU SATO

Institute for Liberal Arts and Sciences, Kyoto University, Kyoto, Japan

ABSTRACT

The Program of the Antarctic Syowa Mesosphere–Stratosphere–Troposphere/Incoherent Scatter (PANSY) radar is a large atmospheric radar located at the Antarctic Syowa Station (69.01°S, 39.59°E). The PANSY radar performed the first incoherent scatter (IS) measurements in the Antarctic region in 2015. Several specific observations were undertaken in 2017 including a 24-h observation of the ionosphere using a peripheral antenna array to suppress interference from the field-aligned irregularities (FAIs). This paper presents the preliminary results derived from the IS measurements using the PANSY radar and the adaptive signal processing techniques to suppress FAIs. The norm-constrained and directionally constrained minimization of power (NC-DCMP) algorithm was applied to the 24-h ionosphere observations by the PANSY radar with a weighting applied to the directional constraint based on the gain differences of the subarrays. When compared with the conventional nonadaptive approach, the number of usable power profiles was increased by about 24% by the gain-weighted NC-DCMP algorithm, suggesting its effectiveness for FAI clutter suppression in ionosphere observations. Furthermore, detection of FAIs using the dedicated antenna array was found valuable in assessing the reliability of estimations of electron density based on VHF-band IS radar data.

1. Introduction

Incoherent scatter (IS) radar is currently the most powerful tool available to investigate the ionosphere because it covers a wide altitudinal range from 100 to 1000 km, and it observes essential ionospheric parameters

such as electron density, ion velocity, ion and electron temperatures, as well as ion compositions (Evans 1969). The number of the IS radars is limited because they have high power demand and require a wide antenna aperture. The technical challenges related to using IS radar have been ongoing for more than five decades. The earliest IS radars, such as those at Millstone Hill (Massachusetts), Jicamarca (Peru), and Arecibo (Puerto Rico) have been operating since the 1960s, whereas the radars of the European Incoherent Scatter Facility (EISCAT) and the middle and upper atmosphere (MU) radar at the Shigaraki MU Observatory in Japan began making

---

observations in the 1980s. More recently, in the 2000s, Advanced Modular Incoherent Scatter Radars (AMISR) have been deployed at Poker Flat (Alaska) and Resolute Bay (Canada). Currently, the new EISCAT radar, EISCAT_3D, is in its development phase but it should be operational by the 2020s (McCrea et al. 2015).

All of the previously listed IS radars are in the Northern Hemisphere and/or the equatorial region. In contrast, the Program of the Antarctic Syowa Mesosphere–Stratosphere–Troposphere/Incoherent Scatter (PANSY) radar is a large atmospheric radar in the Antarctic region, located at Syowa Station (69.01°S, 39.59°E). As its name states, the PANSY radar has the capability of an IS radar. The PANSY radar performed the first IS radar observations in the Antarctic region in 2015. Clearly, observations in the Southern Hemisphere are crucial to revealing global features of both the atmosphere and the ionosphere. In fact, the coupling between the lower and the upper atmospheric layers is expected to show a large difference between the hemispheres, given the strong hemispheric asymmetry of the lower atmosphere. Recent in situ observations by the *Gravity Field and Steady-State Ocean Circulation Explorer* (*GOCE*) satellite have revealed that atmospheric gravity wave activity at altitudes around 250 km shows marked hemispheric differences. These differences are attributed to wave activities within the lower atmosphere and the effects of geospatial topology (Trinh et al. 2018). Atmospheric gravity waves in the ionosphere have been observed as traveling ionospheric disturbances (TIDs) (Hines 1960), which have been investigated using electron density observations of IS radars at high latitudes (Crowley et al. 1984; Nicolls and Heinselman 2007; Medvedev et al. 2015) and midlatitudes (Thome 1964; Oliver et al. 1994) of the Northern Hemisphere. The PANSY radar observation of the electron density of the Antarctic ionosphere is expected to shed new light on the coupling between the lower and the upper atmosphere, as well as providing information on neutral and ionized components through investigation of TIDs.

Although the initial results of the PANSY radar were mainly free from contamination, Sato et al. (2014) highlighted that strong coherent echoes called ionospheric field-aligned irregularities (FAIs) can cause severe interference in observations of incoherent scattering of VHF-band radar. As Fukao et al. (1988) first reported, the MU radar, which uses frequencies similar to the PANSY radar, also observes FAIs because 3-m-scale (or half wavelength) FAIs are predominant. FAIs are irregular structures of high electron density aligned along the geomagnetic field lines generated by plasma instabilities. Radio waves perpendicular to the FAIs are coherently backscattered. Such scattering conditions are satisfied at around 100 km in height and 30° elevation angles at Syowa Station when using the VHF band (Ogawa 1996; Koustov et al. 2001). Therefore, the distance of these FAIs to the radar is greater than 250 km, which causes them to have the same signal range as the IS in the F region observed by the main array at 70° elevation. To suppress interference from these FAIs, the PANSY radar has two special antenna arrays used for adaptive signal processing in cooperation with the main array. These peripheral antenna arrays (hereinafter the FAI array) were not available during the first period of observation in 2015, but they began operating in 2017. Thus, in 2017, several IS measurements were undertaken using the FAI array, including the 24-h ionosphere observation described herein.

In this paper, we present preliminary results of the ionosphere observations using the PANSY radar and we describe the methodologies used to suppress interference from the FAIs. Initially, we review the specifications of the PANSY radar and its supplemental antenna arrays for detecting FAIs. This is followed by a description of two observations made without and with these arrays in 2015 and 2017, respectively. Next, we outline an adaptive signal processing procedure, optimized for the current radar system, and we describe the procedure that has been applied to undertake these observations. We show the results of the application of adaptive signal processing to a 24-h observation by the PANSY radar in 2017, and we discuss its FAI suppression capabilities. Last, we present our concluding remarks concerning the processing of IS radar data with the VHF band.

2. Observations

In this section, the specifications of the PANSY radar system and the details of the two observations made using this radar in 2015 and 2017 are described.

a. Receiver array configuration

The main array of the PANSY radar has 1045 three-element crossed-Yagi antennas arranged in a distributed manner, as shown in Fig. 1 (Sato et al. 2014). In ionosphere observations, all output signals from the antennas in the main array are combined into a single channel. In addition to this main array, the PANSY radar has the FAI array, which comprises a pair of peripheral linear arrays of 12 three-element Yagi antennas configured to observe FAI echoes. Signals from sets of three adjacent antennas in the FAI array are combined in phase, constituting the eight-channel subarray shown as rectangles 2–9 in Fig. 1. Therefore, this configuration can use adaptive signal processing techniques for nine subarrays.
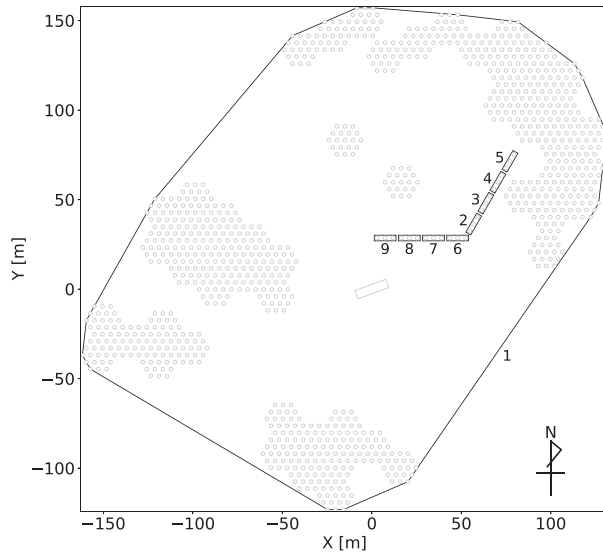
FIG. 1. Antenna positions of the main and FAI arrays of the PANSY radar, and the subarray assignment in the IS observation during 18–19 Dec 2017.

The FAIs are observed in directions where the magnetic field and the line of sight cross perpendicularly. These conditions are satisfied only at the elevation angle of about 30° at Syowa Station. Hence, the antennas of the FAI array are directed to the southeast for channels 2–5, and to the south for channels 6–9, each with an elevation angle of 30°.

The antenna patterns of the main and FAI arrays in a section having an azimuth angle of 135° measured clockwise from north are shown in Fig. 2. Because the number of combined antennas composing the main and FAI arrays is different, the gain difference to the zenith is about 40 dB (Fig. 2).

b. First incoherent scatter measurement in 2015

The first IS measurement using the PANSY radar was made at 1132–1243 local time (LT) 15 May 2015 (LT = UTC + 3). The methods adopted for obtaining both the observation and the estimation of the electron density were based on Sato et al. (1989). The parameters for the radar system are listed in Table 1. During this observation period, signals received from all antennas in the main array were combined in phase. At this time, the FAI array had not been yet installed and therefore further signal processing could not be applied.

The observed height profile of the electron density averaged over the entire period (71 min) and all the beam directions is shown in Fig. 3. The coefficient for converting the echo power into electron density was determined using the critical-frequency f_oF_2 value measured by the on-site ionosonde. The dashed line in
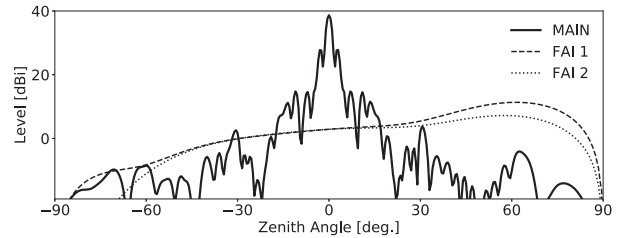

FIG. 2. Antenna patterns of the PANSY radar in the section having an azimuth angle of 135° measured clockwise from north. The solid line (labeled MAIN) is for the main array, the dashed line (FAI 1) is for FAI channels 2–5, and the dotted line (FAI 2) is for FAI channels 6–9.

this figure shows the detectability threshold ($T_d = 3$), which is generally used in atmospheric radars to distinguish a signal from noise (Fukao et al. 2014). As shown by the detectability threshold, the upper limit for IS observation by the PANSY radar is around 700 km. The noise level is estimated using the region above this height.

In this case, the observed height profile followed a reasonable shape for the distribution of the electron density, implying that this measurement was not affected by the FAIs. Although the occurrence of E-region FAIs could not be determined by the on-site ionosonde, this assumption is partially supported by its result for the F region, since no spread F events were recorded during this period. From these observations, the geomagnetic activity measured using the K_p index was considered to be low; that is, it had a K_p value of 2.

c. 24-h continuous observation in 2017

Following the success of the first measurement, a continuous observation of IS was performed from 1312 LT 18 to 1503 LT 19 December 2017. The observation parameters were the same as in 2015 and as listed in Table 1. During the 2017 observation period, the main array was combined in phase, as was done for the 2015 observation. In addition, the FAI array was enabled, although one of the channels in the FAI array ("9" in Fig. 1) was not working because of a system malfunction. Thus, seven channels in the FAI array were available to suppress interference from the FAIs, which yielded eight subarrays.

Figure 4 shows an example of height profiles of electron density measured during 1312–1503 LT 18 December 2017, averaged over all beam directions. The black line shows the output only from the main array and the red line is the signal after adaptive signal processing, as explained in section 3. Other components of the figure are the same as Fig. 3. As described in more detail in section 4, this observation suffered severe interference from FAIs, in contrast to the observation of 2015.

TABLE 1. Parameters for the incoherent scatter measurements made on 15 May 2015 and during 18–19 Dec 2017 by the PANSY radar.

Center frequency	47 MHz
Ranges	140–1230 km
Range resolution Δr	9.6 km
Beam zenith θ	20°
Beam azimuth ϕ	−5°, 85°, 175°, and −95°
Time resolution Δt	40 ms
Pulse compression	7-bit Barker code

Hence, suppression of the FAIs to estimate the true power of the IS using adaptive signal processing techniques was required in this case.

As shown in Fig. 4, the interference of the FAIs can be seen mainly from 700 to 1000 km for this period and adaptive signal processing mitigated these FAIs. For example, around 800 km, the red line (after adaptive signal processing) becomes below or close to the dashed line (the detectability threshold), indicating that the contamination from FAIs was successfully suppressed to reach the noise floor level.

Of course, however, the primary concern of this paper is the performance below this region, and we discuss it in the detailed comparison in section 4. From that perspective, this figure also shows the stability of the technique when FAI interference is weak because the signal after adaptive signal processing (red line) is not changed markedly in comparison with the nonadaptive output (black line) in this region.

3. Signal processing

In this section, the basic methods involved in adaptive beamforming and their implementation during the observation are explained.

a. Signal-processing algorithm

In 2017, continuous observation was performed using the FAI array. Hence, the output signals from all the subarray channels were processed using an adaptive beamforming technique to suppress the FAI echoes.

The method described herein is based on the directionally constrained minimization of power (DCMP) algorithm, with an additional constraint on the norm of the weight vector intended to limit the increase in noise to a designated value. This is known as the norm-constrained DCMP (NC-DCMP) algorithm (Kamio et al. 2004; Nishimura et al. 2012). Furthermore, the gain difference between the main and FAI arrays must be considered to ensure the norm constraint works properly (Hashimoto et al. 2016). The procedures are described below.
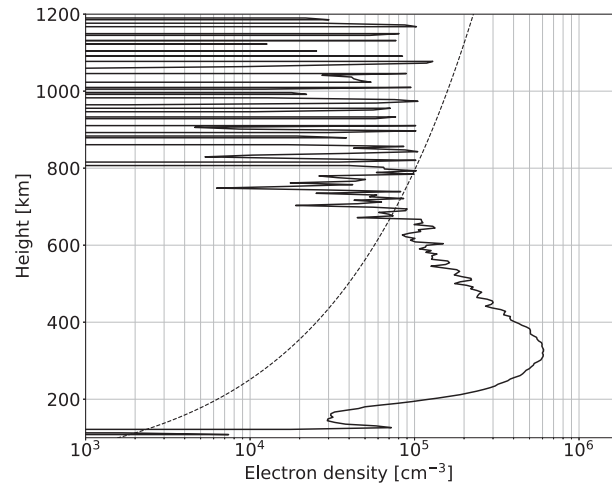

FIG. 3. First electron density profile observed by the PANSY radar on 15 May 2015. The profile is averaged about an hour over all beam directions. The dashed line shows the detectability threshold ($T_d = 3$). The observation parameters are listed in Table 1. The conversion coefficient from echo power to electron density is determined using the f_oF_2 value measured by an on-site ionosonde.

1) NC-DCMP ALGORITHM

The synthesized output of the NC-DCMP algorithm, or Y, is calculated using the following set of equations:

$$Y = \mathbf{W}^H \mathbf{X}, \qquad (1)$$

$$\underset{\mathbf{W}}{\text{minimize}} \ \mathbf{W}^H \mathbf{R} \mathbf{W} \ \text{subject to} \ \mathbf{C}^H \mathbf{W} = 1, \qquad \text{and} \qquad (2)$$

$$\|\mathbf{W}\|^2 \le U, \qquad (3)$$

where $\mathbf{X} = (X_1, X_2, \ldots, X_M)^T$ is a complex time series received by M (=8) spatially distributed receivers, $\mathbf{W}$ is the weight vector, $\mathbf{R} = E(\mathbf{X}\mathbf{X}^H)$ is the covariance matrix, $\mathbf{C}$ is the directional constraint, and U is the norm constraint. Here, $E(\ )$ denotes the ensemble average and $\|\ \|$ represents the Euclidean norm. The norm constraint U is calculated from the designated noise level increase in decibels L_{dB}: $U = 10^{-L_{dB}/10}$.

There is a trade-off between the noise level increase and the clutter suppression capability. However, $L_{dB} = 0.5$ dB is generally used, because it provides reasonable clutter suppression at the cost of small increase in the noise level (Hashimoto et al. 2016). It should also be noted that L_{dB} specifies the worst case, and the actual noise level increase would be smaller if the interference was not severe. Because the algorithm minimizes the total output power including noise and interference, it automatically suppresses the noise level increase in such cases.
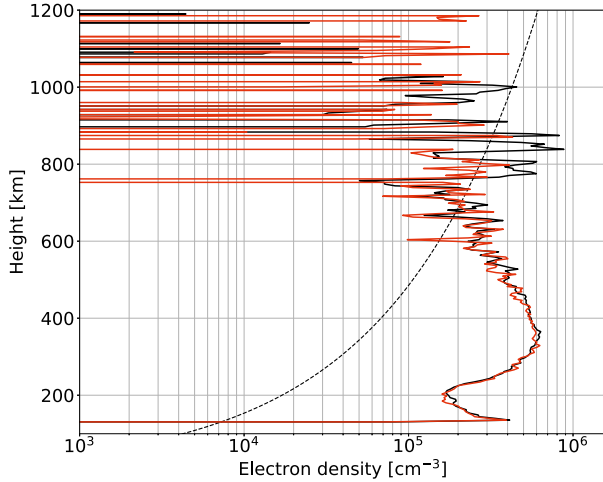
FIG. 4. Example electron density profiles observed by the PANSY radar on 18 Dec 2017. The profiles are averaged about an hour over all beam directions. The black line shows the output only from the main array, and the red line shows the signal after adaptive signal processing, as explained in section 3. Other components are the same as in Fig. 3.

2) GAIN WEIGHTING

The directional constraint $\mathbf{C}$ in Eq. (2) is weighted by the power directional gain of the subarrays $\mathbf{G} = [G_1(\theta_o, \phi_o), G_2(\theta_o, \phi_o), \ldots, G_M(\theta_o, \phi_o)]^T$, to the desired direction (zenith, azimuth) = (θ_o, ϕ_o):

$$C_i = \sqrt{\frac{MG_i(\theta_o, \phi_o)}{\sum_{i=1}^{M} G_i(\theta_o, \phi_o)}} A_i(\theta_o, \phi_o), \qquad (4)$$

$$A_i(\theta, \phi) = \frac{1}{\sqrt{M}} \exp\left[-\mathbf{j}\frac{2\pi}{\lambda}\mathbf{L}_i \cdot \mathbf{V}(\theta, \phi)\right], \quad \text{and} \quad (5)$$

$$\mathbf{V}(\theta, \phi) = (\sin\theta \sin\phi, \sin\theta \cos\phi, \cos\theta)^T,$$

where $\mathbf{j}$ is the imaginary unit, λ is the wavelength, $\mathbf{L}_i$ is the location of the ith receiver, $\mathbf{A}(\theta, \phi)$ is the array manifold vector, and $\mathbf{V}(\theta, \phi)$ is the radial unit vector to the given direction (θ, ϕ). Here, the azimuth angle is measured clockwise from north.

b. Application to the 2017 observation

Both the nonadaptive beamforming and the gain-weighted NC-DCMP algorithm were applied to the eight-channel nonuniform-gain array of the 2017 observation. Hereinafter, the received signal from the south-directed beam is used in the analysis; that is, the desired direction in Eq. (5) is $(\theta_o, \phi_o) = (20°, 175°)$. The main array was already synthesized nonadaptively and assigned to X_1 in Eq. (1), and the other channels from the FAI array were assigned to X_{2-8}.

For the result from the nonadaptive beamforming, we simply used the signal from the first channel, X_1. Conversely, for the result from the NC-DCMP algorithm, we first calculated the optimal weight vector $\mathbf{W}$ through Eqs. (2)–(5). Then, we substituted it in Eq. (1) to obtain the synthesized output with the FAIs suppressed. The parameter set for the NC-DCMP algorithm is mentioned below.

The gain-weighting coefficients $\mathbf{G}$ were $G_1(\theta_o, \phi_o) = 0.9958$ and $G_{2-8}(\theta_o, \phi_o) = 0.0372$, determined using the power directional gain differences to (θ_o, ϕ_o). The norm constraint was set as $U = 1.122$ to limit the increase in the noise to less than 0.5 dB. The covariance matrix $\mathbf{R}$ was calculated using $N = 256$ samples before and after the target time t_i; that is,

$$\mathbf{R}(t_i) = \frac{1}{2N + 1}\sum_{j=i-N}^{i+N} \mathbf{X}(t_j)\mathbf{X}^H(t_j).$$

Consequently, the duration for averaging the covariance matrix was about 21 s. Note that this period is shorter than that used for the mesosphere–stratosphere–troposphere region of about 1 min (Hashimoto et al. 2016), because the correlation time between the IS and the FAI signal is much shorter than between atmospheric echoes and ground clutter.

c. Calculation of the height profiles and meteor rejection

After applying the beamforming technique, height profiles were obtained by averaging the received power. For every N_a (=204) samples (~8.16 s), the DC offset was removed and the power was averaged for each range to obtain a single height profile $P(r)$, in which r is the height index of the profile.

To remove contamination from meteors and other artifacts, the following thresholding procedure was applied successively. Initially, for every N_1 (=22) height profiles (~3 min), the mean noise level $\overline{P}_{N_1}(r)$ was estimated for each range. Then, each profile $P(r)$ in the set was tested to ascertain whether the following condition was satisfied:

$$\left[r \middle| P(r) \geq \left(1 + \frac{T_d}{\sqrt{N_a}}\right)\overline{P}_{N_1}(r)\right] = \emptyset, \qquad (6)$$

where $T_d = 7$ is the constant used for thresholding in this study and Ø denotes an empty set. Only profiles satisfying Eq. (6) were used in the incoherent integrations. Here, the left-hand side of Eq. (6) indicates a set of height indices where the signal level exceeds the detectability threshold, and $T_d = 7$ was chosen experimentally to balance the impact of the number of discarded profiles and

remaining meteor echoes on the smoothness of the averaged profiles. Last, N_2 (=5) successive sets of meteor-rejected profiles passing the test in Eq. (6) were integrated to calculate 15-min-averaged profiles. However, if the number of averaged profiles was less than 70% of the total number of profiles N_1N_2 (=110) (i.e., less than 77 in a 15-min interval) then the entire set of profiles was discarded to avoid unreliable estimation. Herein, this procedure is called meteor rejection.

d. Detection of field-aligned irregularities

The procedures for applying the proposed signal processing techniques to the 2017 observation have been explained above. For quantitative discussion in section 4 regarding the FAI suppression capability of the proposed method, the occurrence of FAIs is first considered.

The occurrence of FAIs was determined using the received signals from the FAI array. As shown in Fig. 2, the directivity gains of the FAI channels are optimized for directions where FAIs appear, with no response in the main beam direction. Therefore, all echoes observed by the FAI channels can be considered FAIs or meteors. Here, we did not distinguish between these two echo sources because it is advantageous to suppress meteor echoes when they are observed by the FAI channels.

For each FAI channel, averaged power profiles without applying the meteor rejection procedure, $P^{(i)}(r)$ (i = 2, ... , 8), were first calculated with N_1N_2 incoherent integrations. Then, the mean noise level of the ith channel in a 15-min interval, $\overline{P}^{(i)}_{N_1N_2}(r)$, was calculated from the profile $P^{(i)}(r)$ to build the detectability threshold in the same manner as Eq. (6). Hence, any ranges satisfying the following condition were assumed to have FAIs:

$$\left[r \left| P^{(i)}(r) \geq \left(1 + \frac{T_d}{\sqrt{N_a N_1 N_2}} \right) \overline{P}^{(i)}_{N_1N_2}(r) \right. \right] \neq \varnothing. \quad (7)$$

Note that the FAI array is not beamformed, and Eq. (7) is satisfied if any one of the FAI channels exceeds the detectability threshold.

4. Results and discussion

Figure 5 shows time series of 15-min-averaged power profiles and FAI occurrences from the south-directed beam during the continuous observation period of 2017. The panels of this figure show the raw power profiles (Fig. 5a; i.e., those obtained from nonadaptive beamforming without meteor rejection), power profiles obtained using the conventional method (Fig. 5b; i.e.,

nonadaptive beamforming with meteor rejection), power profiles obtained using the proposed method (Fig. 5c; i.e., the gain-weighted NC-DCMP algorithm with meteor rejection), and the occurrence of FAIs during the observation period (Fig. 5d). The horizontal axis of each panel is time (LT) and the vertical axis is range in km multiplied by cos20°, which can be interpreted as actual heights for the results from the main array (i.e., in Figs.5a–c). In Figs.5a–c, colors indicate the intensity of the estimated power profiles against the noise level in decibels. In Fig. 5d, the black coloring shows the time and height of FAI occurrence, estimated using the procedure described in section 3d. Note that these FAIs are considered to originate in the E region because the perpendicular condition is only satisfied therein using the VHF band, as mentioned in section 1. This panel also contains data from the on-site ionosonde, illustrating the occurrence of spread F events by the red marking.

As shown in Figs. 5b and 5c, the number of profiles discarded by the meteor rejection process is reduced when the NC-DCMP algorithm is used. The ratio of rejected profiles to total profiles in Fig. 5b is 35.78%, while in Fig. 5c it is 11.92%, representing an improvement of 23.85%. The average loss of signals by the NC-DCMP algorithm is about 0.02 dB, which is calculated from the difference between Figs. 5b and 5c using the times and ranges without the black hatching in Fig. 5d (i.e., the data in which the FAIs are not detected). Note that this is sufficiently small value when compared with the maximum allowable increase of the noise level (0.5 dB) designated in section 3b, indicating the stability of the proposed method.

As compared with Fig. 5b, the profiles in Fig. 5c have fewer temporal discontinuities in received power, especially during daytime (e.g., 1200–1500 LT on both days). For example, an unnatural step discontinuity at 1245 LT in Fig. 5b is mitigated, and some missing profiles are restored in Fig. 5c. In these intervals, Figs. 5b and 5c differ markedly from Fig. 5a, reflecting the meteor rejection process, although almost no FAIs or meteors were detected above 250 km, as indicated in Fig. 5d. This is due to a lack of sensitivity in the FAI array, making it difficult to detect weak echoes above this height using the given detectability threshold. Nevertheless, the proposed gain-weighted NC-DCMP algorithm did suppress weak clutter to obtain diurnal variation in the background IS with less rejected profiles and ignorable loss of desired signals in comparison with existing techniques. This is one of the main advantages of adaptive signal processing.
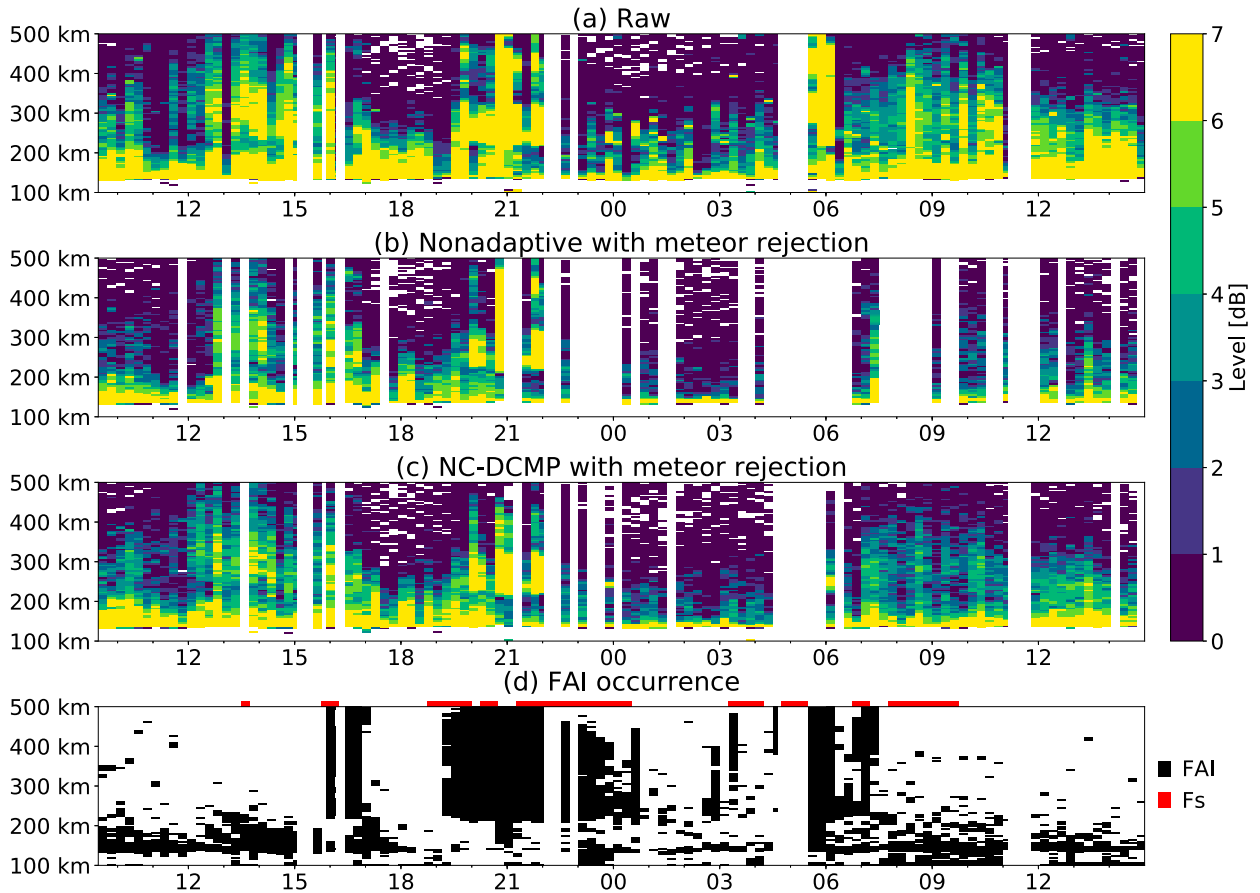
FIG. 5. Time series of 15-min-averaged power profiles for the south-directed beam during the continuous observation period of 2017: (a) raw power profiles, (b) power profiles obtained using nonadaptive beamforming with meteor rejection, (c) power profiles obtained using the NC-DCMP algorithm with meteor rejection, and (d) occurrence of FAIs estimated using channels 2–8 (label FAI); also shown in (d) is the occurrence of spread F events determined by the on-site ionosonde (label Fs). The horizontal axis of each panel is time (LT), and the vertical axis is range multiplied by cos20°.

Interestingly, very strong FAIs (e.g., during 1900–2200 LT 18 December 2017) were not suppressed fully by the adaptive signal processing, as shown in Fig. 5c. Even in such cases, we can still detect FAIs using the FAI array, and we can mark these contaminated records as requiring caution in their analysis. Hence, this method is more robust in estimating the electron density than using signals only from the main array. Furthermore, although the on-site ionosonde detected only the existence of spread F events as shown by the red marking in Fig. 5d, which is not necessarily related to the E-region FAIs, the FAI array directly observed the E-region FAIs and provided a broader coverage in both temporal and spatial distributions. The importance of the dedicated FAI array is also supported by this result, since the ionosonde and FAI array observe different targets using different frequencies (i.e., the FAIs in F and E regions using HF and VHF bands, respectively).

From the above discussion, we conclude that the FAI array is effective for assessing the reliability of estimations of electron density based on VHF-band IS radar data.

5. Summary and conclusions

This paper presents the initial results of ionosphere observations by the PANSY radar, which uses an adaptive signal processing algorithm for signals from auxiliary antenna arrays to suppress FAI clutter. The gain-weighted NC-DCMP algorithm applied to the eight-channel subarray configuration of the PANSY radar suppressed echoes from FAIs and meteors with the sufficiently small loss of signals of about 0.02 dB on average. This increased the number of usable power profiles by 23.85% when compared with conventional nonadaptive beamforming. In addition, even when strong FAIs could not be suppressed fully, we can

still use the output from the FAI array to detect FAIs and to reject contaminated records, which improves the reliability of the estimations of electron density based on VHF-band IS radar data.

From these results, we conclude that using a subarray dedicated to FAI observation, together with adaptive signal processing, is valuable for ionosphere observations in the Antarctic region. Furthermore, the gain-weighted NC-DCMP algorithm is acknowledged as a satisfactory workable solution for the PANSY radar. This proposed method and configuration are planned to be applied to the other types of IS radar observations with the PANSY radar (e.g., multipulse observations used to measure ion drift speeds and temperatures) in the future.

REFERENCES

Crowley, G., T. B. Jones, T. R. Robinson, N. M. Wade, and O. Holt, 1984: Determination of the vertical neutral temperature and wind profiles using EISCAT and HF Doppler radar. *J. Atmos. Terr. Phys.*, **46**, 501–507, https://doi.org/10.1016/0021-9169(84)90068-0.

Evans, J. V., 1969: Theory and practice of ionosphere study by Thomson scatter radar. *Proc. IEEE*, **57**, 496–530, https://doi.org/10.1109/PROC.1969.7005.

Fukao, S., J. McClure, A. Ito, T. Sato, I. Kimura, T. Tsuda, and S. Kato, 1988: First VHF radar observation of midlatitude F-region field-aligned irregularities. *Geophys. Res. Lett.*, **15**, 768–771, https://doi.org/10.1029/GL015i008p00768.

——, K. Hamazu, and R. J. Doviak, 2014: *Radar for Meteorological and Atmospheric Observations*. Springer, 537 pp., https://doi.org/10.1007/978-4-431-54334-3.

Hashimoto, T., K. Nishimura, and T. Sato, 2016: Adaptive sidelobe cancellation technique for atmospheric radars containing arrays with nonuniform gain. *IEICE Trans. Commun.*, **E99**, 2583–2591, https://doi.org/10.1587/transcom.2016EBP3047.

Hines, C. O., 1960: Internal atmospheric gravity waves at ionospheric heights. *Can. J. Phys.*, **38**, 1441–1481, https://doi.org/10.1139/p60-150.

Kamio, K., K. Nishimura, and T. Sato, 2004: Adaptive sidelobe control for clutter rejection of atmospheric radars. *Ann. Geophys.*, **22**, 4005–4012, https://doi.org/10.5194/angeo-22-4005-2004.

Koustov, A. V., K. Igarashi, D. André, K. Ohtaka, N. Sato, H. Yamagishi, and A. Yukimatu, 2001: Observations of 50- and 12-MHz auroral coherent echoes at the Antarctic Syowa station. *J. Geophys. Res.*, **106**, 12 875–12 887, https://doi.org/10.1029/2000JA000165.

McCrea, I., and Coauthors, 2015: The science case for the EISCAT_3D radar. *Prog. Earth Planet. Sci.*, **2**, 21, https://doi.org/10.1186/s40645-015-0051-8.

Medvedev, A., K. Ratovsky, M. Tolstikov, S. Alsatkin, and A. Shcherbakov, 2015: A statistical study of internal gravity wave characteristics using the combined Irkutsk Incoherent Scatter Radar and Digisonde data. *J. Atmos. Sol. Terr. Phys.*, **132**, 13–21, https://doi.org/10.1016/j.jastp.2015.06.012.

Nicolls, M. J., and C. J. Heinselman, 2007: Three-dimensional measurements of traveling ionospheric disturbances with the Poker Flat Incoherent Scatter Radar. *Geophys. Res. Lett.*, **34**, L21104, https://doi.org/10.1029/2007GL031506.

Nishimura, K., T. Nakamura, T. Sato, and K. Sato, 2012: Adaptive beamforming technique for accurate vertical wind measurements with multichannel MST radar. *J. Atmos. Oceanic Technol.*, **29**, 1769–1775, https://doi.org/10.1175/JTECH-D-11-00211.1.

Ogawa, T., 1996: Radar observations of ionospheric irregularities at Syowa Station, Antarctica: A brief overview. *Ann. Geophys.*, **14**, 1454–1461, https://doi.org/10.1007/s00585-996-1454-z.

Oliver, W. L., S. Fukao, Y. Yamamoto, T. Takami, M. D. Yamanaka, M. Yamamoto, T. Nakamura, and T. Tsuda, 1994: Middle and upper atmosphere radar observations of ionospheric density gradients produced by gravity wave packets. *J. Geophys. Res.*, **99**, 6321–6329, https://doi.org/10.1029/94JA00171.

Sato, K., and Coauthors, 2014: Program of the Antarctic Syowa MST/IS radar (PANSY). *J. Atmos. Sol. Terr. Phys.*, **118A**, 2–15, https://doi.org/10.1016/j.jastp.2013.08.022.

Sato, T., I. Atsuo, W. L. Oliver, S. Fukao, T. Tsuda, S. Kato, and I. Kimura, 1989: Ionospheric incoherent scatter measurements with the middle and upper atmosphere radar: Techniques and capability. *Radio Sci.*, **24**, 85–98, https://doi.org/10.1029/RS024i001p00085.

Thome, G. D., 1964: Incoherent scatter observations of traveling ionospheric disturbances. *J. Geophys. Res.*, **69**, 4047–4049, https://doi.org/10.1029/JZ069i019p04047.

Trinh, Q. T., M. Ern, E. Doornbos, P. Preusse, and M. Riese, 2018: Satellite observations of middle atmosphere–thermosphere vertical coupling by gravity waves. *Ann. Geophys.*, **36**, 425–444, https://doi.org/10.5194/angeo-36-425-2018.